Poroelasticity of Cartilage at the Nanoscale

Hadi Tavakoli Nia,[†] Lin Han,[‡] Yang Li,[§] Christine Ortiz,[‡] and Alan Grodzinsky[†§¶‖*]
[†]Department of Mechanical Engineering, [‡]Department of Materials Science and Engineering, [§]Department of Biological Engineering, [¶]Department of Electrical Engineering and Computer Science, and [‖]Center for Biomedical Engineering, Massachusetts Institute of Technology, Cambridge, Massachusetts

ABSTRACT Atomic-force-microscopy-based oscillatory loading was used in conjunction with finite element modeling to quantify and predict the frequency-dependent mechanical properties of the superficial zone of young bovine articular cartilage at deformation amplitudes, δ, of ~15 nm; i.e., at macromolecular length scales. Using a spherical probe tip ($R \sim 12.5\ \mu$m), the magnitude of the dynamic complex indentation modulus, $|E^*|$, and phase angle, φ, between the force and tip displacement sinusoids, were measured in the frequency range $f \sim 0.2$–130 Hz at an offset indentation depth of $\delta_0 \sim 3\ \mu$m. The experimentally measured $|E^*|$ and φ corresponded well with that predicted by a fibril-reinforced poroelastic model over a three-decade frequency range. The peak frequency of phase angle, f_{peak}, was observed to scale linearly with the inverse square of the contact distance between probe tip and cartilage, $1/d^2$, as predicted by linear poroelasticity theory. The dynamic mechanical properties were observed to be independent of the deformation amplitude in the range $\delta = 7$–50 nm. Hence, these results suggest that poroelasticity was the dominant mechanism underlying the frequency-dependent mechanical behavior observed at these nanoscale deformations. These findings enable ongoing investigations of the nanoscale progression of matrix pathology in tissue-level disease.

INTRODUCTION

Poroelasticity of cartilage, including fluid pressurization and the viscous drag of the flow through the porous extracellular matrix (ECM), plays an important role in load-bearing (1), energy dissipation and self-stiffening (i.e., increase in the dynamic stiffness of cartilage with increasing compression frequency) (2,3), solute and fluid transport (4), lubrication (5,6) and mechanotransduction (7). Poroelasticity and intrinsic viscoelasticity (8) of the ECM macromolecules are the two main mechanisms of energy dissipation and time-dependent behavior in cartilage. Poroelastic energy dissipation originates from fluid-solid frictional interactions due to fluid pressurization and viscous drag through the porous ECM (9,10). Intrinsic viscoelastic dissipation is related to the relaxation and reconfiguration of ECM macromolecules including the collagen fibrillar network, negatively charged aggrecan aggregates, and associated matrix molecules (8,11–13). Instrumented and atomic-force-microscopy (AFM)-based indentation studies of intact cartilage tissue and the chondrocyte-cell-associated matrix have begun to elucidate the relation between matrix molecular structure and mechanical behavior (14–22). These studies have primarily focused on the elasticity of the tissue as quantified using single-phase elastic contact models such as the Hertzian (23) and Oliver-Pharr approaches (24). Consequently, although the poroviscoelastic behavior of cartilage has been extensively studied at the micro- (25,26) and macroscale (8,27), time-dependent behavior and energy dissipation mechanisms of the cartilage ECM at the nanoscale are not well understood (21,22).

Cartilage tissue-level biomechanical properties are determined by the tissue's fibrillar collagen network and the negatively charged glycosaminoglycan (GAG) side chains of aggrecan. To obtain insights into the nanoscale contribution of such macromolecules to the time-dependent mechanical behavior of the ECM, AFM-based force relaxation and dynamic oscillatory indentation were recently performed on young bovine cartilage (22) and tissue engineered cell-associated matrix (21). Using displacement amplitudes of ~2–50 nm in conjunction with scaling arguments, it was suggested that poroelasticity is the dominant mechanism under these loading conditions (21,22). In our previous work (22), a Hertzian model was used to describe the time-dependent nanomechanics of native (untreated) and proteoglycan-depleted cartilage disks, and to quantify such properties as the indentation modulus, the force-relaxation time constant, and the magnitude and phase of the complex dynamic modulus. $|E^*|$ was observed to increase with frequency from 0.22 ± 0.02 MPa at 1 Hz to 0.77 ± 0.10 MPa at 316 Hz, and this increase was accompanied by an increase in phase angle δ. The quantification of the nanoscale dynamic mechanical properties of cartilage opens up great opportunities for early diagnosis of tissue alteration and disease (16) and for investigation of the role of other important proteins in ECM by comparing data from wild-type and knockout mice models (28), which are challenging to quantify by traditional methods due to their small size and irregular shape.

In this study, we expanded significantly upon our previous work, first by using AFM-based dynamic oscillatory indentation in conjunction with a judicious choice of the AFM-probe radius ($R \sim 12.5\ \mu$m) to obtain a full-spectrum experimental frequency response, i.e., from the

Submitted June 11, 2011, and accepted for publication September 6, 2011.

*Correspondence: alg@mit.edu

Editor: Peter Hinterdorfer.

0006-3495/11/11/2304/10 $2.00

doi: 10.1016/j.bpj.2011.09.011

low-frequency (equilibrium) compressive limit up to the high-frequency (instantaneous stiffness) limit, which would include the midfrequency range in which energy dissipation should peak. Second, we used the observed length scale dependence of the dynamic response of cartilage to test the hypothesis that poroelasticity is the dominant mechanism governing the time/frequency-dependent behavior of cartilage at the nanoscale. Third, we used two different widely used poroelastic models, isotropic (10) and fibril-reinforced (29), to predict the observed frequency-dependent nanomechanical behavior of cartilage. This fibril-reinforced composite model was constructed to simulate the structure and properties of the cartilage ECM components, i.e., collagen and aggrecan (25,30). By accounting for the fibrillar collagen network, parametric study has been carried out on the important material parameters that determine the poroelastic energy dissipation at the nanometer-level deformation amplitudes, including the elastic modulus, E_m, and hydraulic permeability, k, of the nonfibrillar matrix (mainly aggrecan), and the elastic modulus, E_f, of the fibrils. These parameters have been quantified for the superficial zone of young bovine cartilage. Quantifying the nanoscale poroelastic properties of tissue such as the elastic moduli of fibrillar and nonfibrillar matrix and their hydraulic permeability will serve to relate alteration in the tissue's mechanical properties to its molecular structure in different contexts, such as the initiation and progression of osteoarthritis (16), the contribution of important proteins in ECM other than the well-studied macromolecules such as collagen and aggrecan (28), and the development of tissue-engineered matrices (21).

MATERIALS AND METHODS

Sample preparation

Cartilage disks with an intact superficial zone (9 mm in diameter × 1 mm thick) were harvested from the femoropatellar grooves of 1–2-week-old bovine calves (Fig. 1 *a*), as described previously (31), and maintained in sterile phosphate-buffered saline (PBS, without Mg^{2+} and Ca^{2+}) with protease inhibitors (Complete Protease cocktail tablets, Roche Applied Science, Indianapolis, IN) at 4°C for <24 h before testing. All the measurements were performed in near-physiological PBS (137 mM NaCl, 10 mM phosphate, 2.7 mM KCl, pH 7.4) at ambient temperature (25°C).

AFM-based dynamic oscillatory nanoindentation

Experiments were performed using cartilage disks harvested from three joints (from three separate animals). Four disks were harvested from each joint, and indentations at four different locations were performed on each disk. Dynamic oscillatory indentation tests were performed using the MultiMode AFM with a PicoForce piezo and Nanoscope IV controller via the force mode (Veeco, Santa Barbra, CA) (Fig. 1 *b*). Gold-coated polystyrene colloidal probe tips (end radius (R)~12.5 μm; nominal spring constant (k) ~4.0 N/m; Novascan, Ames, IA) were functionalized with a neutral hydroxyl-terminated self-assembled monolayer (OH-SAM, 11-mecaptoudecanol, Sigma-Aldrich, St. Louis, MO). The cantilever deflection sensitivity (nm/V) was calibrated on a hard mica surface, where the cantilever deflection equals the z-piezo displacement in the contact region. The thermal oscillation method was applied to determine the cantilever spring constant for each probe tip (32). The applied piezo displacement profile for each indentation test was composed of an initial ~3 μm indentation and subsequent force relaxation, followed by sinusoidal displacements applied over a frequency range of $f = 0.2$–130 Hz. A function generator (Model 645, Berkeley Nucleonics, San Rafael, CA) connected to the PicoForce piezo controller was used to apply the sinusoidal displacements via the sweep mode in the form of an exponential downchirp signal (high- to low-frequency, shown schematically in Fig. 1 *c*) for a duration of 100 s for each frequency sweep. The amplitude of the

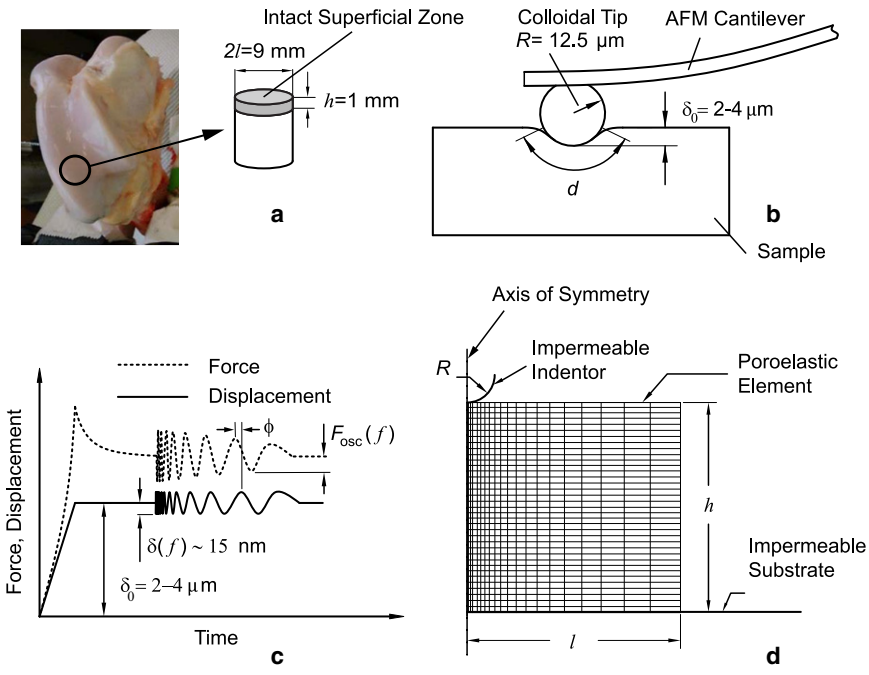

FIGURE 1 (*a*) Samples were harvested from the femoropatellar grooves of 1- to 2-week-old bovine calves. (*b*) Compressive deformations were applied using AFM probe tips with a probe diameter of $R = 12.5$ μm. (*c*) The deformation profile consisted of an initial preindentation of $\delta_0 = 2$–4 μm followed by sinusoidal displacements with an amplitude of $\delta = 15$ nm superimposed on the the preindentation, δ_0. The displacement frequency was swept from $f = 0.2$–130 Hz. (*d*) The finite element simulation is shown schematically for an impermeable indentor and substrate.

sinusoidal displacements, $\delta = 15$ nm, was chosen to be much less than the initial offset indentation, $\delta_0 \sim 3$ μm ($\delta << \delta_0$). Control experiments were first performed using a mica sample at the same z-piezo displacement frequencies and amplitudes as for system calibration (22). At low frequencies (<10 Hz), the amplitude and phase of the z-piezo deformation/voltage ratio is constant as a function of frequency, and no correction is needed. At higher frequencies (>10 Hz), correction for the magnitude and phase of the stiffness was performed based on the ratio between z-displacement and z-voltage (Fig. S4 in the Supporting Material), which is the continuous version of the discrete analysis described in our previous study (22). The probe displacement was obtained by subtracting the deflection from the z-piezo signal. The corresponding force exerted on the probe was calculated as the product of the deflection signal and the cantilever spring constant. In a separate test, the frequency sweep method was compared independently to results obtained by application of discrete frequencies, using 10 cycles at each frequency over the entire range of interest. The close agreement between the results of the frequency sweep and discrete frequency loading confirmed the appropriateness of the sweep method, which was then used for all of the experiments presented here.

Four disks were harvested from each joint (one disk each from the anterior and posterior aspects of the medial and lateral surfaces of the femoropatellar groove), and oscillatory indentations were performed at four different locations on each disk. The dynamic stiffness (magnitude and phase) was measured for these four tests per disk, and a mean of the corresponding material property values (E_m, E_f, and k) was assigned to each disk. The mean $\pm$ SE of the material properties of each joint were then calculated from these four disks (i.e., $n = 4$). The averaged material property values over all three joints were then computed (i.e., mean $\pm$ SE, $n = 3$).

Data analysis and calculation of magnitude and phase of the complex modulus

A discrete Fourier transform (DFT) was used to obtain the fundamental frequency components of the z-piezo and deflection signals, from which the amplitude of the oscillatory force of the probe, F_{osc}, and the oscillatory displacement of the probe, δ (Fig. 1 *c*), were calculated at each frequency, f. The sampling rate of the DFT was $f_s = 4000$ Hz (i.e., at least 10 times greater than the highest loading frequency used). The magnitude of the dynamic complex indentation modulus at each frequency was then obtained as (33)

$$|E^*(f)| = \frac{F_{osc}(f)}{\delta(f)} \frac{1}{2(R\delta_0)^{1/2}}, \quad (1)$$

where R is the probe radius. F_{osc}/δ was normalized as above, based on a Taylor series expansion of the Hertz model to account for the spherical probe tip geometry (33). The phase angle $\phi(f)$ was then calculated as the phase between the fundamental sinusoidal components of F_{osc} and δ (shown schematically in Fig. 1 *c*). Tanϕ is then related to the energy dissipation (34). After obtaining the dynamic modulus as a complex number in frequency domain, the amplitude and phase were each smoothed using a moving average. This procedure was carried out on the logarithmically spaced signals via an algorithm defined such that the start and end frequencies (f_s and f_e, respectively) of the window for the moving average are related by $\log(f_e) - \log(f_s) = 0.05$); i.e., the window size was 5% of a logarithmic decade. All the data processing was performed using MATLAB (The MathWorks, Natick, MA).

Poroelastic finite element modeling

Isotropic poroelastic model

The isotropic model was implemented using the soil mechanics capacity of the general-purpose commercial finite element software ABAQUS (Version 6.9, Simulia, Providence, RI) for the configuration shown in Fig. 1 *d*. Because of the symmetry of the problem, the specimen was modeled using axisymmetric, poroelastic elements (CAX4P). The probe-tip indenter was modeled as a rigid surface since the spherical tip is much stiffer than cartilage. The probe tip was assigned a displacement history as described above (see Fig. 1 *c*), and a zero-displacement boundary condition was assumed at the lower cartilage-substrate interface. The indenter and the substrate surface were assumed to be impermeable to fluid flow. Since tip friction was predicted to have negligible effects on the nanoindentation load-displacement curves using the developed finite element model (see Fig. S6 and Gupta et al. (25)), the indenter-cartilage contact region was assumed to be frictionless. The reduced friction and surface adhesion that resulted from functionalizing the tip with OH-SAM further supported this modeling assumption. The pore pressure was set to zero at the top surface of the cartilage (excluding the indenter contact surface) and the side surfaces of the cartilage to simulate free draining of the interstitial fluid from the cartilage at those surfaces. The height h and radius l of the sample were set to be much larger than the indenter contact distance, d ($l = h = 100$ μm >> $d/2 \sim 8$ μm; see Fig. 1, *b* and *d*), to simulate an infinite domain on the radius and depth of the cartilage disk sample. The relevant mechanical properties in this isotropic model are Young's modulus, E, the hydraulic permeability, k, and Poisson's ratio, ν.

Fibril-reinforced poroelastic model

A fibril-reinforced poroelastic model (30) was also tested, in which cartilage is approximated as a composite composed of an isotropic nonfibrillar matrix (representing the proteoglycan constituents; same element as used in the isotropic model), a fibril network (representing collagen fibrils), and a fluid phase (representing the water/electrolyte solution). The mechanical properties of the nonfibrillar matrix are assumed to be the Young's modulus, E_m, Poisson's ratio, ν, and the hydraulic permeability, k. The fibril network is represented by the Young's modulus E_f, which is assumed to be independent of strain. In the fibril-reinforced model, as a first approximation, it is assumed that the fibers resist only tension, and the compressive modulus for the fibers is set to zero (29). The deformation, fluid velocity, and pore pressure fields caused by the initial offset indentation depth ($\delta_0 \sim 3$ μm) and subsequent dynamic compression were largely confined to the top ~100 μm of superficial zone cartilage, i.e., a distance of around eight probe radii (see the discussion of Fig. 5, below). Therefore, the measured dynamic moduli largely reflect the material properties of the superficial zone.

Calculation of poroelastic material properties

In the isotropic model (10,27), the Young's modulus, E, was determined directly from the low-frequency modulus, E_L. The hydraulic permeability, k, was determined from the peak frequency of the phase angle, and Poisson's ratio, ν, was varied from 0 to 0.45 to obtain the best fit.

In the fibril-reinforced model, the poroelastic properties, E_m, E_f, and k, were obtained from the best fit of the model to the experimental data (smoothed magnitude, $|E^*|$, and phase, ϕ, of the dynamic modulus in frequency domain). First, the low-frequency asymptote of the model was fit to that of the experimental data by varying E_m (It will be shown below in the parametric study that varying the other parameters—E_f, k, and the Poisson's ratio, ν—did not affect the low-frequency asymptote). Then, with E_m fixed, the high-frequency asymptote was found to depend only on E_f (see the parametric study section in Results). Therefore, E_f was obtained by fitting the high-frequency asymptote of the model to that of the experimental data. Finally, the hydraulic permeability, k, was obtained by matching the frequency of the peak of the theoretical phase angle to that of the data, since varying the permeability only shifted the frequency dependence of $|E^*|$ and ϕ. Throughout this study, we used a value for Poisson's ratio of $\nu = 0.1$, the same value measured previously for 1- to 2-week old bovine femoropatellar groove cartilage similar to that used in this study (35). E_m, E_f, and k were calculated from the results of experiments

performed on cartilage disks harvested from three joints (from three separate animals).

RESULTS

Dynamic nanoindentation response of cartilage

The magnitude and phase angle, $|E^*|$ and ϕ, of the dynamic complex indentation modulus measured versus frequency is shown in Fig. 2 for a typical cartilage disk. The solid black line corresponds to the mean value of frequency sweeps at 10 different locations on one disk, and the dashed black lines are the 95% confidence intervals for these 10 locations. For the 12.5-μm-radius AFM probe tip used in this study, the peak in phase angle, f_{peak}, was observed to occur typically at the characteristic frequency f_{peak} ~ 20 Hz (Fig. 2 *b*). At low frequencies, $f << f_{peak}$, $|E^*|$ approached an asymptotic value defined as E_L (Fig. 2 *a*), which corresponds to the equilibrium elastic mechanical response of the cartilage specimen in the absence of rate processes. At high frequencies, $f >> f_{peak}$, $|E^*|$ approached an asymptotic (frequency-independent) value defined as E_H. In subsequent experiments, performed to estimate the constituent mechanical properties of disks from all three animals (see Table 1 below, which will be discussed in more detail later) as detailed in the Methods, low- and high-frequency asymptotes of $|E^*|$, as well as a peak in the phase angle, ϕ, were clearly observed for each frequency sweep on each disk specimen, qualitatively similar in appearance to that of Fig. 2.

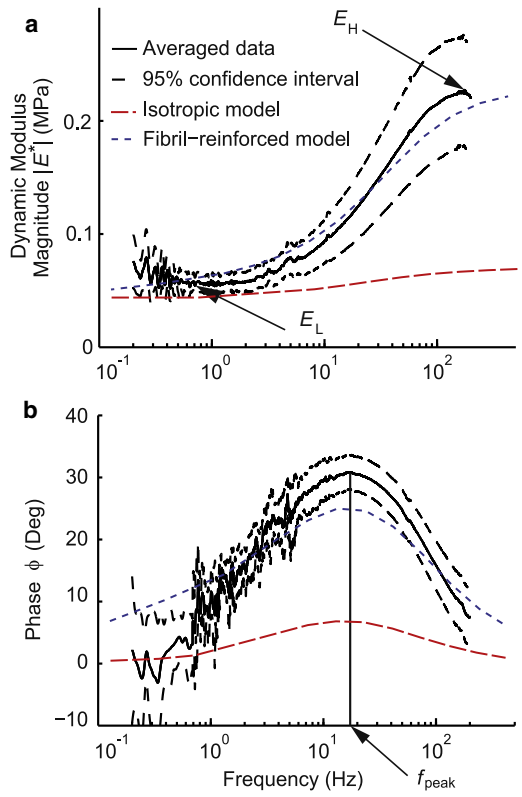

FIGURE 2 (*a*) The mean value and 95% confidence intervals for the magnitude of the dynamic indentation modulus, $|E^*|$, is shown as a function of frequency for $n = 10$ independent indentation sites on one typical disk. The moduli E_L and E_H represent the low-frequency and high-frequency asymptotes, respectively, of the modulus curve. (*b*) The mean value and 95% confidence intervals for the phase angle of the dynamic modulus versus frequency. The characteristic frequency at which the phase peaks is denoted by f_{peak}. At low and high frequencies the phase angle approaches zero. The behavior predicted by an isotropic (dashed red line) and a fibril-reinforced (dotted blue line) poroelastic finite element model are shown for the magnitude and phase of the dynamic modulus. The material parameters obtained from the best fit of the isotropic model to the data are $E = 0.032$ MPa, $k = 9.1 \times 10^{-14}$ m^4/N·s, and $\nu = 0$. The material parameters obtained from the best fit of the fibril-reinforced model are: $E_m = 0.032$ MPa, $E_f = 0.29$ MPa, and $k = 1.3 \times 10^{-14}$ m^4/N·s, with ν taken to be 0.1 based on measurements reported for similar bovine calf cartilage in the literature (35).

The length scale dependence of dynamic nanomechanical properties suggests that poroelasticity is the dominant dissipation mechanism at the nanoscale

Taking advantage of the fact that the dissipation due to flow-dependent poroelasticity depends on the characteristic length scale of the fluid flow, whereas the dissipation due to intrinsic viscoelasticity is theoretically length scale-independent, we investigate the contribution of poroelasticity in the observed nanoscale frequency-dependent behavior of cartilage. Based on the linear poroelasticity theory (9), the characteristic poroelastic diffusion time is $\tau_p \sim [L^2/(Hk)]$, where H is the longitudinal (confined-compression) modulus, k the hydraulic permeability, and L the characteristic length over which fluid flows, and where, therefore, $L \sim d$ (see Fig. 3 *c*, *inset*) based on the contact distance between the indenter and sample corresponding to the probe tip geometry and load magnitude of the nanoindentation experiment. The characteristic frequency, f_{peak}, governing the dynamic response is the inverse of τ_p, and is defined as (22,27)

$$f_{peak} \propto \frac{kH}{d^2}, \tag{2}$$

where f_{peak} is the peak frequency of the phase angle (e.g., Fig. 2 *b*). We experimentally tested the relation between

TABLE 1 Poroelastic properties of bovine calf femoropatellar groove cartilage disks harvested with intact superficial zone

Joint (animal) no.	E_m (MPa)	E_f (MPa)	k (m^4/N·s) $\times 10^{-15}$
1	0.054 ± 0.011	0.30 ± 0.05	7.79 ± 1.51
2	0.101 ± 0.024	0.56 ± 0.15	11.60 ± 2.44
3	0.073 ± 0.020	0.39 ± 0.05	10.64 ± 2.41
Mean ± SE	0.076 ± 0.007	0.42 ± 0.08	10.01 ± 1.14

E_m = Young's modulus of the nonfibrillar matrix; E_f = Young's modulus of the fibrillar network; k = hydraulic permeability. Disks ($n = 4$) were tested from each of $N = 3$ joints. First, for each disk, values were computed as the mean ± SD from $m = 4$ different locations on that disk. The mean ± SE was then computed for the $n = 4$ disks harvested from each joint. Finally, the mean ± SE was obtained from the $N = 3$ joints.

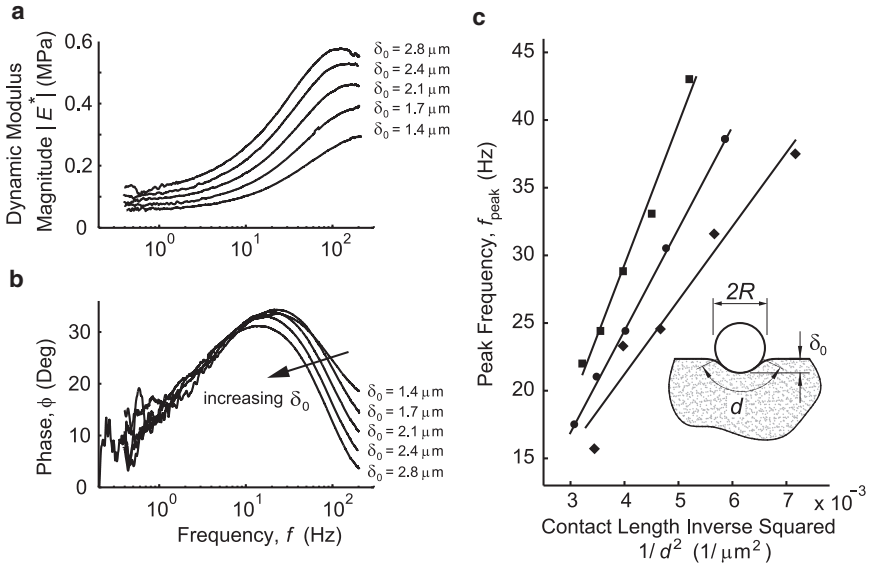

FIGURE 3 (*a* and *b*) Magnitude (*a*) and phase (*b*) of the dynamic indentation modulus of cartilage measured with increasing indentation depths, δ_0, and, as a result, increasing contact distances, *d*, for indentation at a single typical location. (*c*) The peak frequency, f_{peak}, decreased with increasing contact distance, *d*. f_{peak} is plotted as a function of the inverse square of the contact distance, $1/d^2$, for five sequential increases in *d* performed at three different locations (each line corresponding to one of the locations). The best-fit linear regression lines between f_{peak} and $1/d^2$ (the minimum value of the goodness of fit, R^2, was 0.949 for all 16 locations) confirming this relation between f_{peak} and $1/d^2$ suggest that poroelasticity is the dominant mechanism in the observed dynamic response at the nanoscale.

f_{peak} and *d* in Eq. 2 by varying the initial offset indentation depth, δ_0, in a manner that would alter the contact distance, *d*. With δ_0 initially set to 1.4, 1.7, 2.1, 2.4, and finally 2.8 μm at a given location, a dynamic indentation frequency sweep was applied at each δ_0, and $|E^*|$ and ϕ were plotted as a function of frequency. An increase in δ_0 caused a shift in the measured $|E^*|$ and ϕ toward lower frequencies (e.g., the experiment of Fig. 3, *a* and *b*, performed at a single location on one disk). The peak in the phase angle was then plotted versus $1/d^2$ (e.g., the three different locations on one disk shown in Fig. 3 *c*), where *d* was calculated from the contact geometry as $d = 2R\cos^{-1}[(R - \delta_0)/R]$. To check the linearity between f_{peak} and $1/d^2$, which is predicted by linear poroelasticity theory, a straight line was fit to the data of f_{peak} vs. $1/d^2$ at each value of δ_0 at each indentation location, and the goodness of fit, R^2, was calculated. This process was repeated on each of the four different locations on each of the four disks from each of the three joints. For all 48 locations, excellent linearity was observed, as the minimum value of R^2 was 0.949. The difference in the slopes of the lines in Fig. 3 *c* corresponds to spatial variations in the mechanical properties (e.g., *H* and *k*) at each indentation location.

Fibril-reinforced poroelastic model predicts the dynamic modulus more efficiently than an isotropic poroelastic model

Given the results of Fig. 3, which strongly suggest the dominance of poroelastic behavior governing the nanomechanical response of cartilage, we then tested the ability of both an isotropic and a fibril-reinforced poroelastic theoretical model to predict the measured dynamic response. In the isotropic model, varying the hydraulic permeability shifted the frequency response to higher/lower frequencies but did not change the values of the maximum phase angle or the high-frequency asymptotic modulus, E_H. For the above parameter ranges, the maximum phase angle predicted by the isotropic model was $\phi_{max} = 8°$ (Fig. 2 *b*, *dashed red line*), whereas the maximum phase angle measured experimentally was in the range 25–50°. The high-frequency/low-frequency ratio asymptotic modulus magnitudes, E_H/E_L, predicted by the isotropic model was $E_H/E_L < 2$ (Fig. 2 *a*, *dashed red line*), whereas the observed E_H/E_L was in the range 4–10. In contrast, the fibril-reinforced model better predicted the frequency dependence of $|E^*|$ and ϕ (Fig. 2, *dotted blue lines*). By increasing the E_f/E_m ratio, the maximum value of the phase angle, as well as the ratio of E_H/E_L, increased to values closer to those measured experimentally (Fig. 2). Finally, we note that Eq. 2 for f_{peak} was also found to hold for both the fibril-reinforced and isotropic poroelastic models using finite element simulations described above.

Parametric study of the fibril-reinforced poroelastic model

At very low frequencies, the contribution of fluid flow is negligible and the mechanical response is governed by the purely elastic response of the material. Consequently, the low-frequency modulus is equal to the Young's modulus of the nonfibrillar matrix, E_m. This was verified in simulations using values of E_m from 0.01 to 0.05 MPa and observing that $E_L = E_m$ in the low-frequency limit (Fig. 4 *a*). With values of E_f, ν, and *k* fixed, an increase in E_m decreased the maximum phase angle and shifted the peak frequency toward higher frequencies (Fig. 4 *b*).

With E_m, ν, and *k* held constant, an increase in E_f should further reinforce the poroelastic matrix by the tension-resisting fibril network, resulting in a higher high-frequency

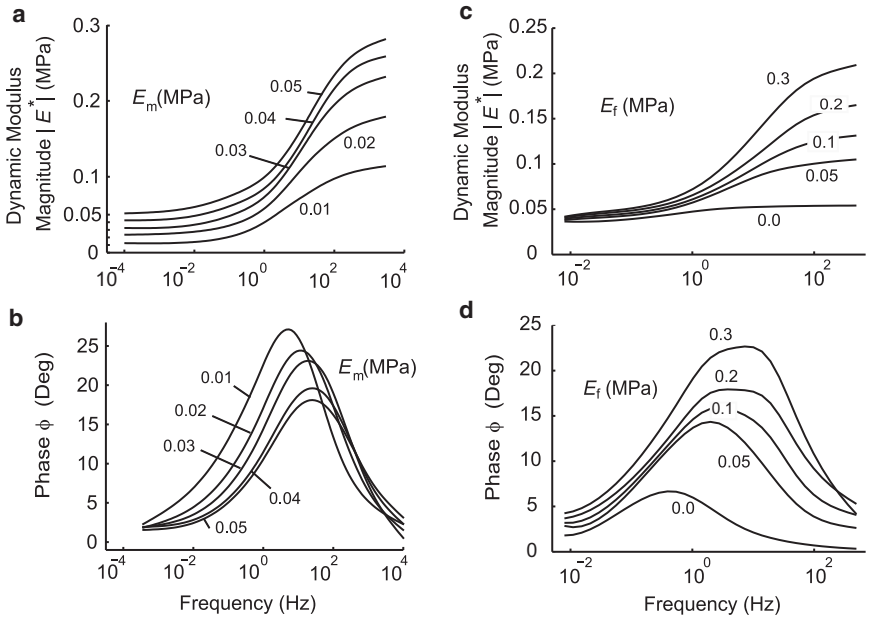

FIGURE 4 (*a* and *b*) Parametric study of the dynamic response of the fibril-reinforced model by varying the Young's modulus of the nonfibrillar matrix, E_m. The other parameter values are fixed at: $E_f = 0.1$ MPa, $k = 2 \times 10^{-14}$ m^4/N·s, and $\nu = 0.1$ (*c* and *d*) Parametric study of the dynamic response by varying the Young's modulus of the fibril network, E_f. The other parameter values are fixed at $E_m = 0.03$ MPa, $k = 2 \times 10^{-14}$ m^4/N·s, and $\nu = 0.1$.

modulus, E_H, at the same time leaving E_L unaffected at the value of the given Young's modulus of nonfibrillar matrix, E_m. Simulations using the fibril-reinforced model showed exactly this trend (Fig. 4 *c*). The increase in E_f also resulted in a higher value of f_{peak} and a shift in f_{peak} to the higher frequency (Fig. 4 *d*).

The variation of the drained Poisson's ratio of the nonfibrillar matrix over the range of values reported in the literature had only a small effect on the dynamic response (see Fig. S1). Thus, we used a Poisson's ratio value of $\nu = 0.1$, as described above (35). Variation in the hydraulic permeability, k, resulted in a proportional frequency shift of the dynamic response, leaving the low- and high-frequency moduli and the maximum phase angle unaffected, as expected.

Poroelastic properties of superficial-zone cartilage ECM constituents estimated from dynamic nanoindentation

By fitting the predictions of the fibril-reinforced poroelastic model to the data from all three animals, values for E_m, E_f, and k (assuming $\nu = 0.1$) for superficial-zone tissue were estimated (Table 1). The low-frequency modulus, E_L, directly determined the Young's modulus, E_m. Since the E_H/E_L ratio is only a function of E_f/E_m, E_f was readily calculated after E_m was determined. Having found E_m and E_f, k was found from the observed value of f_{peak}, since the variation in k only resulted in a frequency shift of the dynamic response, leaving the high- and low-frequency moduli unaffected. For each joint, four disks are harvested (two from the medial and two from the lateral parts), and four indentations at different locations are performed on each plug. The reported values (Table 1) for each joint are based on $n = 4$ disks, where the values for each disk are the average of the corresponding values over four different locations on the disk. The reported value for all joints is based on $n = 3$ joints, where the value for each joint is that obtained from the average of the 16 indentations.

Intratissue fluid velocity and fluid pressure profiles at low and high frequencies

Using the mean values of the poroelastic properties in Table 1 ($E_m = 0.076$ MPa, $E_f = 0.42$ MPa, $k = 10.01 \times 10^{-15}$ m^4/N·s, and $\nu = 0.1$), the spatial profiles of intratissue fluid velocity and pressure in the region ~75 μm below the probe tip were calculated using the fibril-reinforced model for selected times during a deformation cycle of the probe tip (Fig. 5). These computations were performed for frequencies of $f = 3$ Hz and $f = 70$ Hz, corresponding to frequencies below and above f_{peak}. The magnitude of the velocity field is shown at times $t = 0$, $T/4$, $T/2$, and $3T/4$, where T is the period of the corresponding frequency (Fig. 5, *a–d* and *a′–d′*). For $f << f_{peak}$, the fluid velocity caused by probe tip motion is very small, except for the very thin region immediately below the probe tip. The velocity field at higher frequencies is larger in magnitude, and the fluid flows deeper into the tissue compared to flows caused by low-frequency oscillation. For high frequencies, the flow extends downward to ~50 μm below the probe tip, i.e., about four times the probe radius ($R = 12.5$ μm). Therefore, the material properties reported in Table 1 are the effective properties of the superficialmost ~50 μm of tissue. For both high and low frequencies, the fluid velocity magnitude is highest at the interface between the tip and

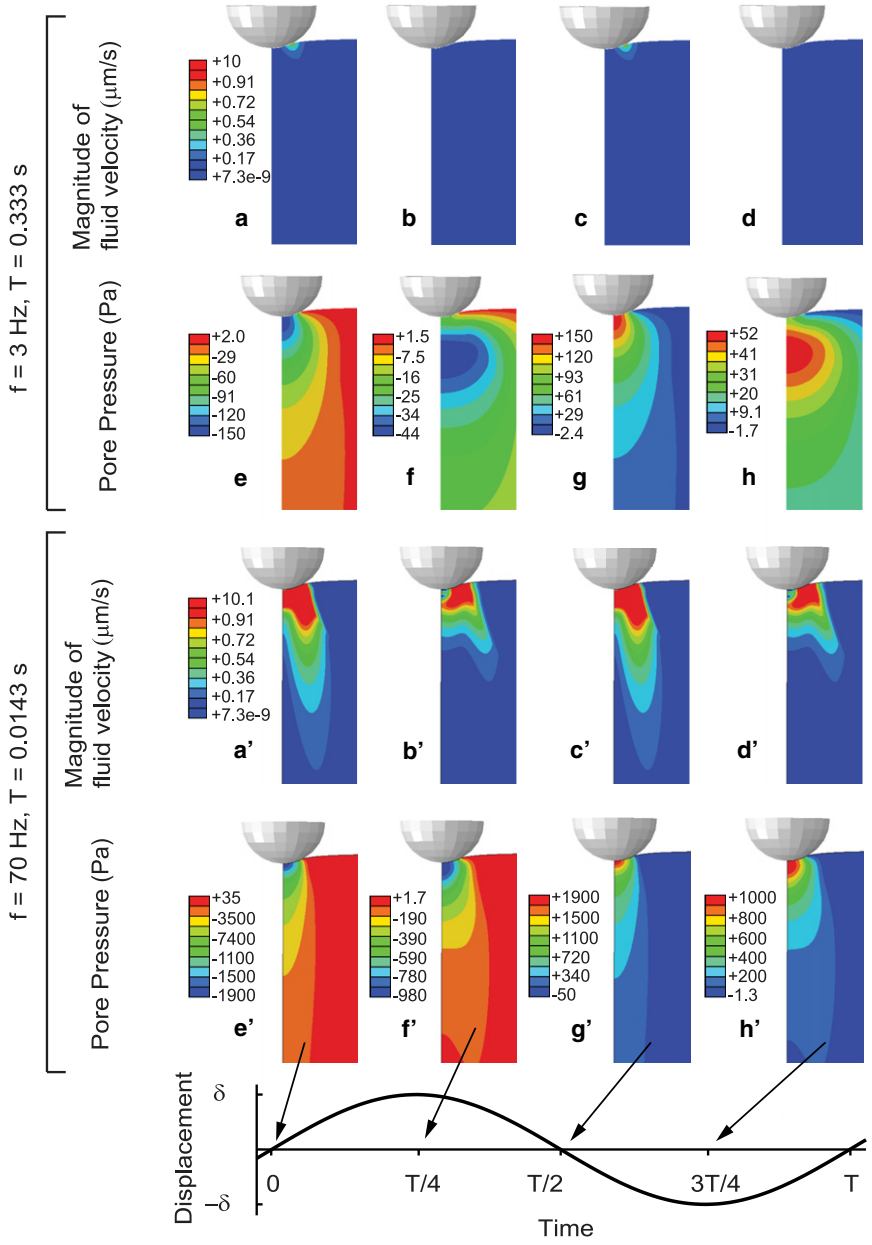

FIGURE 5 Fluid velocity magnitude and pore pressure computed from the fibril-reinforced model based on parameter values in Table 1. Fluid velocity magnitude is shown for low frequencies, $f = 3$ Hz (*a*–*d*), and high frequencies, $f = 70$ Hz (a'–d'). Pore pressure is shown for low frequencies, $f = 3$ Hz (*e*–*h*), and high frequencies, $f = 70$ Hz (e'–h'). The fluid velocity and pore pressure are compared at four different times over a full cycle, i.e., $t = 0$, $T/4$, $T/2$, and $3T/4$, where T is the period of the corresponding frequency.

sample (Fig. 5), and it attains maximum value at the time when the tip starts a compression cycle. The corresponding pore pressure field (Fig. 5, *e*–*h* and e'–h') attains a maximum value just below the tip, at the symmetry line. The pressure is zero at all the free surfaces of the sample where the fluid can drain freely. Similar to fluid velocity, the pore pressure extends deeper into the tissue at higher frequencies.

DISCUSSION

In this study, AFM-based oscillatory compression was used in conjunction with poroelastic finite element modeling to measure and predict the frequency-dependent mechanical behavior of superficial zone cartilage. The previously established methodology of Han et al. (22) was expanded to enable measurement of the full poroelastic response over a three-decade frequency range: both low- and high-frequency asymptotes in the magnitude of the dynamic modulus (corresponding to equilibrium and instantaneous responses, respectively) were clearly observed, as was the peak in phase lag (related to the peak in energy dissipation). Since the nanoindentation frequency response of a hydrated tissue depends on tissue mechanical properties and geometric considerations (e.g., tip radius, R, and offset indentation depth, δ_0), the choice of R in this study was critically important in enabling the measurement of the full frequency response. Previous attempts at achieving the peak phase lag were unsuccessful in macroscale (31) and nanoscale (22)

deformation due to limits associated with the characteristic length scales and frequency ranges of the test machines.

The low-frequency limit of the dynamic modulus is the equilibrium modulus, since deformations are so slow that the fluid flow becomes negligible. At high frequencies, the fluid cannot move quickly enough relative to the solid network, and the response is equivalent to that of an incompressible material with the same shear modulus as that at low frequencies (36). At frequencies between these limits, the poroelastic response of the cartilage dominates and the phase angle attains a peak value in the region of the inflection frequency of the dynamic modulus, $|E^*|$ (Fig. 2). Thus, the parameters E_H, E_L, and f_{peak} form a complete set to compare the predictions of the poroelastic finite element model to estimate the intrinsic material properties of cartilage.

To test the hypothesis that poroelasticity is the dominant mechanism underlying the dynamic nanoindentation response, we first compared the length scale dependence of the measured f_{peak} and then compared the predictions of poroelastic theory to the measured indentation response over the entire frequency range. The length scale dependence of f_{peak} was tested by varying the contact distance, d, experimentally (Fig. 3), and linear poroelasticity theory was indeed able to predict this scaling dependence (Eq. 2). Comparing isotropic and fibril-reinforced poroelastic models, the fibril-reinforced model was found to better predict the magnitude and phase of the dynamic modulus over the entire frequency range of interest. Due to complex architecture of the collagen network, cartilage is highly anisotropic and has different properties in tension and compression. At higher frequencies, the fluid pressurization generates dynamic radial expansion of the matrix where the reinforcement of the matrix plays an important role in the dynamic response. The fibril-reinforced model is one of the models widely used to describe this biomechanical attribute of cartilage (29). In this model, the fibril network resists tension and, superimposed with the isotropic nonfibrillar matrix, determines the mechanical stiffness of the material. Comparing the isotropic poroelastic model (10) with the fibril-reinforced one (29) in the indentation geometry of interest, we found that the fibril-reinforced model better predicts the dynamic response of the cartilage at the nanoscale (Fig. 2), as has been observed for unconfined compression at the tissue scale (30). The remaining discrepancy between the theoretical model and data are likely due to additional complex behavior of cartilage ECM, including anisotropy of the elastic constants and permeability, strain-dependent permeability, fibril orientation, strain-rate-dependent fibril stiffness, and the intrinsic viscoelasticity of the ECM macromolecules.

The frequency dependence of the storage and loss moduli, an alternative representation of the measured force and displacement data, was also studied (see, e.g., Fig. S5 for the storage and loss moduli corresponding to the data of Fig. 2). Similar to the frequency dependence of the stiffness magnitude, the storage modulus increases monotonically with frequency between low- and high-frequency asymptotes. The frequency response of the loss modulus is similar to that of the stiffness phase angle, and is related to energy dissipation. A peak in the loss modulus similar to that of the phase angle response was observed; however, the peak in loss modulus occurred at ~50 Hz, whereas the peak in the stiffness phase angle was ~20 Hz.

Using the fibril-reinforced model, we then estimated the intrinsic material properties of immature bovine cartilage with an intact superficial zone, including the Young's modulus of the nonfibrillar matrix, E_m, the Young's modulus of the fibrillar network, E_f, and the hydraulic permeability, k (Table 1). Analysis (Fig. 5) showed that the material properties so calculated correspond to those of the most superficial ~100 μm of tissue, i.e., the properties of the superficial zone of cartilage. The depth dependence of the equilibrium longitudinal (confined-compression) modulus, H, of bovine articular cartilage has been reported previously (37); the measured value for the most superficial 125 μm of tissue was $H \sim 0.1$ MPa, which is in reasonable agreement with the Young's modulus $E_m = 0.08$ MPa obtained here (see Table 1; for $\nu = 0.1$, $H \sim E_m$ within 2% error). In addition, the hydraulic permeability measured by dynamic nanoindentation ($k \sim 10.1 \pm 1.14 \times 10^{-14}$ m^4/N·s, Table 1) is also consistent with the known lower glycosaminoglycan content (and thus higher permeability) of the superficial zone.

Thus, the ability of our approach for measuring the intrinsic material properties of cartilage at high spatial and depth resolutions appears particularly useful in isolating the properties of superficial zone cartilage, which is known to be the region subject to the earliest degradation in osteoarthritic disease (38). The variation in the mechanical properties measured from location to location, disk to disk, and joint to joint is most likely due to the known heterogeneity of cartilage (39), associated with variations in the biochemical composition and spatial orientation of matrix macromolecules. Although the presence of a cell directly under the probe tip may also contribute to the variation in measured property values (17), we speculate that the sparse distribution of cells in the superficial zone (40) together with many indentation repetitions at different sites would likely minimize such effects (for more details, see Fig. S7).

One advantage of the method developed to measure the poroelastic properties of the cartilage is the ability to capture the time-dependent behavior at both short and long timescales. Human and animal cartilages experience compressive deformations over a very wide range of amplitudes and frequencies, depending on various activities of living. Quick running and jumping results in cartilage impact strains of a few percent, and the resulting strain rates can correspond to frequencies as high as the kHz range. Conversely, resting after loading leads to very slow stress

relaxation rates, corresponding to larger deformations and frequencies as low as mHz. This represents a range in frequency of 6 orders of magnitude, with deformations in the whole joint from nano- to macroscale. In this study, we measured the dynamic response of cartilage over all the possible frequencies within the limitations of the instrument (0.2–130 Hz) with nanoscale deformation amplitudes. The increase in stiffness and dissipation occurs at high frequencies (short-time loading), which correspond to impact loading. This behavior has previously been investigated in macroscale deformations, whereas this work focused on nanoscale deformation.

Ongoing studies using this approach are focused on measurement and modeling of electrokinetic interactions in charged tissue and gels such as cartilage. The presence of electrokinetic streaming potentials constitutes direct evidence of local intratissue fluid flow. Mechanical deformation of the hydrated extracellular matrix causes a flow of interstitial fluid and fluid-entrained counterions relative to the fixed charge group of proteoglycans. This fluid flow is driven by compression-induced pressure gradients, as simulated diagrammatically in Fig. 5. Thus, fluid convection of counterions tends to separate these ions from the oppositely charged molecules of the matrix, thereby producing an electric field collinear with the fluid flow and proportional to the fluid velocity at each position within the matrix, which has been characterized at the tissue scale (3,41). These ongoing studies should enable understanding of the electrokinetics of cartilage at the nanoscale.

This method may also be relevant for diagnostics of cartilage pathology. Although stiffness may change between healthy and diseased tissue by a factor of 2 or 3 (42), we recently found that the hydraulic permeability of biochemically degraded tissue increased by an order of magnitude (not discussed here), which can be quantitatively measured by the change in the frequency peak of the phase angle. Therefore, this study sets the groundwork for ongoing investigations of poroelasticity of tissue during osteoarthritis-like disease progression by characterizing the poroelastic behavior of cartilage at nanoscale deformations.

CONCLUSION

Here, we used AFM-based dynamic oscillatory compression (frequency range, $f \sim 0.1$–100 Hz; amplitude, $\delta \sim 15$ nm; indentation depth, $\delta_0 \sim 3\ \mu$m) in conjunction with poroelastic finite element modeling to quantify and predict the frequency-dependent mechanical behavior of cartilage. We observed the full poroelastic response of the cartilage over the frequency range of three decades, i.e., we clearly observed the low- and high-frequency asymptotes in the magnitude of the dynamic modulus (corresponding to equilibrium and instantaneous responses, respectively), as well as the peak in the phase angle (corresponding to the peak in energy dissipation). First, by defining the characteristic frequency f_{peak} as the frequency at which the phase angle peaks, we showed that f_{peak} scales linearly with the inverse square of the contact distance, $1/d^2$, where the contact distance, d, is the characteristic distance over which the fluid flows. Second, we observed that the magnitude of the dynamic modulus, $|E^*|$, and the phase angle, ϕ, correspond well to that predicted by the fibril-reinforced model. And third, the dynamic mechanical properties were observed to be independent of the deformation amplitude in the range $\delta = 7$–50 nm over the entire frequency spectrum of interest, as predicted by linear poroelasticity theory. The above evidence suggests that poroelasticity is the dominant mechanism underlying the time-dependent mechanical behavior at nanoscale deformations.

SUPPORTING MATERIAL

Seven figures and references are available at http://www.biophysj.org/biophysj/supplemental/S0006-3495(11)01065-4.

The authors thank the Institute for Soldier Nanotechnologies at Massachusetts Institute of Technology for use of instruments.

This work was supported by the National Science Foundation (grant CMMI-0758651) and the National Institutes of Health (grant AR033236).

REFERENCES

1. Mow, V. C., M. H. Holmes, and W. M. Lai. 1984. Fluid transport and mechanical properties of articular cartilage: a review. *J. Biomech.* 17:377–394.
2. Lee, R. C., E. H. Frank, …, D. K. Roylance. 1981. Oscillatory compressional behavior of articular-cartilage and its associated electro-mechanical properties. *J. Biomech. Eng.* 103:280–292.
3. Frank, E. H., and A. J. Grodzinsky. 1987. Cartilage electromechanics—I. Electrokinetic transduction and the effects of electrolyte pH and ionic strength. *J. Biomech.* 20:615–627.
4. Maroudas, A. 1975. Biophysical chemistry of cartilaginous tissues with special reference to solute and fluid transport. *Biorheology.* 12:233–248.
5. McCutchen, C. W. 1962. The frictional properties of animal joints. *Wear.* 5:1–17.
6. Walker, P. S., D. Dowson, …, V. Wright. 1968. "Boosted lubrication" in synovial joints by fluid entrapment and enrichment. *Ann. Rheum. Dis.* 27:512–520.
7. Quinn, T. M., A. J. Grodzinsky, …, E. B. Hunziker. 1998. Mechanical compression alters proteoglycan deposition and matrix deformation around individual cells in cartilage explants. *J. Cell Sci.* 111:573–583.
8. Mak, A. F. 1986. The apparent viscoelastic behavior of articular cartilage—the contributions from the intrinsic matrix viscoelasticity and interstitial fluid flows. *J. Biomech. Eng.* 108:123–130.
9. Grodzinsky, A. J. 2011. Fields, Forces, and Flows in Biological Systems. Garland Science, New York 259–272.
10. Mow, V. C., S. C. Kuei, …, C. G. Armstrong. 1980. Biphasic creep and stress relaxation of articular cartilage in compression? Theory and experiments. *J. Biomech. Eng.* 102:73–84.
11. Huang, C. Y., V. C. Mow, and G. A. Ateshian. 2001. The role of flow-independent viscoelasticity in the biphasic tensile and compressive responses of articular cartilage. *J. Biomech. Eng.* 123:410–417.
12. Fyhrie, D. P., and J. R. Barone. 2003. Polymer dynamics as a mechanistic model for the flow-independent viscoelasticity of cartilage. *J. Biomech. Eng.* 125:578–584.

13. June, R. K., S. Ly, and D. P. Fyhrie. 2009. Cartilage stress-relaxation proceeds slower at higher compressive strains. *Arch. Biochem. Biophys.* 483:75–80.

14. Allen, D. M., and J. J. Mao. 2004. Heterogeneous nanostructural and nanoelastic properties of pericellular and interterritorial matrices of chondrocytes by atomic force microscopy. *J. Struct. Biol.* 145: 196–204.

15. Darling, E. M., R. E. Wilusz, …, F. Guilak. 2010. Spatial mapping of the biomechanical properties of the pericellular matrix of articular cartilage measured in situ via atomic force microscopy. *Biophys. J.* 98:2848–2856.

16. Stolz, M., R. Gottardi, …, U. Aebi. 2009. Early detection of aging cartilage and osteoarthritis in mice and patient samples using atomic force microscopy. *Nat. Nanotechnol.* 4:186–192.

17. Roduit, C., S. Sekatski, …, S. Kasas. 2009. Stiffness tomography by atomic force microscopy. *Biophys. J.* 97:674–677.

18. Loparic, M., D. Wirz, …, M. Stolz. 2010. Micro- and nanomechanical analysis of articular cartilage by indentation-type atomic force microscopy: validation with a gel-microfiber composite. *Biophys. J.* 98: 2731–2740.

19. Park, S., K. D. Costa, …, K. S. Hong. 2009. Mechanical properties of bovine articular cartilage under microscale indentation loading from atomic force microscopy. *Proc. Inst. Mech. Eng. H.* 223:339–347.

20. Li, C., L. A. Pruitt, and K. B. King. 2006. Nanoindentation differentiates tissue-scale functional properties of native articular cartilage. *J. Biomed. Mater. Res. A.* 78:729–738.

21. Lee, B. B., L. Han, …, A. J. Grodzinsky. 2010. Dynamic mechanical properties of the tissue-engineered matrix associated with individual chondrocytes. *J. Biomech.* 43:469–476.

22. Han, L., E. H. Frank, …, C. Ortiz. 2011. Time-dependent nanomechanics of cartilage. *Biophys. J.* 100:1846–1854.

23. Landau, L. D., and E. M. Lifshitz. 1959. Theory of Elasticity. Pergamon Press, London.

24. Oliver, W. C., and G. M. Pharr. 1992. Improved technique for determining hardness and elastic modulus using load and displacement sensing indentation experiments. *J. Mater. Res.* 7:1564–1583.

25. Gupta, S., J. Lin, …, L. Pruitt. 2009. A fiber reinforced poroelastic model of nanoindentation of porcine costal cartilage: a combined experimental and finite element approach. *J. Mech. Behav. Biomed. Mater.* 2:326–337, discussion 337–338.

26. Miller, G. J., and E. F. Morgan. 2010. Use of microindentation to characterize the mechanical properties of articular cartilage: comparison of biphasic material properties across length scales. *Osteoarthritis Cartilage.* 18:1051–1057.

27. Mak, A. F., W. M. Lai, and V. C. Mow. 1987. Biphasic indentation of articular cartilage—I. Theoretical analysis. *J. Biomech.* 20:703–714.

28. Glasson, S. S., R. Askew, …, E. A. Morris. 2005. Deletion of active ADAMTS5 prevents cartilage degradation in a murine model of osteoarthritis. *Nature.* 434:644–648.

29. Soulhat, J., M. D. Buschmann, and A. Shirazi-Adl. 1999. A fibril-network-reinforced biphasic model of cartilage in unconfined compression. *J. Biomech. Eng.* 121:340–347.

30. Li, L. P., J. Soulhat, …, A. Shirazi-Adl. 1999. Nonlinear analysis of cartilage in unconfined ramp compression using a fibril reinforced poroelastic model. *Clin. Biomech. (Bristol, Avon).* 14:673–682.

31. Kim, Y. J., L. J. Bonassar, and A. J. Grodzinsky. 1995. The role of cartilage streaming potential, fluid flow and pressure in the stimulation of chondrocyte biosynthesis during dynamic compression. *J. Biomech.* 28:1055–1066.

32. Hutter, J. L., and J. Bechhoefer. 1993. Calibration of atomic force microscope tips. *Rev. Sci. Instrum.* 64:1868.

33. Mahaffy, R. E., S. Park, …, C. K. Shih. 2004. Quantitative analysis of the viscoelastic properties of thin regions of fibroblasts using atomic force microscopy. *Biophys. J.* 86:1777–1793.

34. Lakes, R. S. 1999. Viscoelastic Solids. CRC Press, Boca Raton, FL.

35. Buschmann, M. D., Y. J. Kim, …, A. J. Grodzinsky. 1999. Stimulation of aggrecan synthesis in cartilage explants by cyclic loading is localized to regions of high interstitial fluid flow. *Arch. Biochem. Biophys.* 366:1–7.

36. Ateshian, G. A., B. J. Ellis, and J. A. Weiss. 2007. Equivalence between short-time biphasic and incompressible elastic material responses. *J. Biomech. Eng.* 129:405–412.

37. Schinagl, R. M., D. Gurskis, …, R. L. Sah. 1997. Depth-dependent confined compression modulus of full-thickness bovine articular cartilage. *J. Orthop. Res.* 15:499–506.

38. Hollander, A. P., I. Pidoux, …, A. R. Poole. 1995. Damage to type II collagen in aging and osteoarthritis starts at the articular surface, originates around chondrocytes, and extends into the cartilage with progressive degeneration. *J. Clin. Invest.* 96:2859–2869.

39. Xia, Y., J. B. Moody, …, G. Lust. 2002. Characteristics of topographical heterogeneity of articular cartilage over the joint surface of a humeral head. *Osteoarthritis Cartilage.* 10:370–380.

40. Wong, M., P. Wuethrich, …, E. Hunziker. 1996. Zone-specific cell biosynthetic activity in mature bovine articular cartilage: a new method using confocal microscopic stereology and quantitative autoradiography. *J. Orthop. Res.* 14:424–432.

41. Frank, E. H., and A. J. Grodzinsky. 1987. Cartilage electromechanics—II. A continuum model of cartilage electrokinetics and correlation with experiments. *J. Biomech.* 20:629–639.

42. Guilak, F., A. Ratcliffe, …, V. C. Mow. 1994. Mechanical and biochemical changes in the superficial zone of articular cartilage in canine experimental osteoarthritis. *J. Orthop. Res.* 12:474–484.